Sensitivity Study of Multiconstellation GNSS-R to Soil Moisture and Surface Roughness Using FY-3E GNOS-II Data

Zhongmin Ma, Adriano Camps, Hyuk Park, Shuangcheng Zhang, Xiaojun Li, Wigneron J.-P.

Sensitivity Study of Multiconstellation GNSS-R to Soil Moisture and Surface Roughness Using FY-3E GNOS-II Data

Zhongmin Ma, *Student Member, IEEE*, Adriano Camps, *Fellow, IEEE*, Hyuk Park, *Senior Member, IEEE*, Shuangcheng Zhang, Xiaojun Li, and Jean-Pierre Wigneron, *Fellow, IEEE*

***Abstract*—The potential of spaceborne global navigation satellite system reflectometry (GNSS-R) to retrieve a variety of geophysical parameters has already been demonstrated in numerous studies. In 2021, China successfully launched the Fengyun-3E (FY-3E) polar orbit satellite. It carries the GNSS occultation sounder-II (GNOS-II) that can simultaneously receive reflected signals from the global positioning system, BeiDou, and Galileo constellations. Multiconstellation measurement significantly reduces the revisit time of the spaceborne GNSS-R data. This offers the possibility to study the sensitivity of the reflected signals from multi-GNSS constellations to surface parameters at global scale. The main objective of this article is to analyze the sensitivity of FY-3E GNOS-II surface reflectivity (SR) to soil moisture (SM), vegetation, and surface roughness for different GNSS constellations, and different incidence angles. FY-3E data from May 2023 to October 2023 were collected along with SM data from the soil moisture active passive (SMAP). The SMAP static auxiliary surface roughness parameter SMAP-h was also collected for subsequent comparisons. Furthermore, the effect of vegetation in the reflected signal was accounted for using the SM and ocean salinity INRA-CESBIO *L*-band vegetation optical depth. Afterward, for each GNSS constellation, the SR was binned as a function of SM, SMAP-h, and incidence angle. The results indicate that the sensitivity for the different GNSS constellations is consistent, showing similar behavior. Moreover, this study also reports for the first time the experimentally computed sensitivity of FY-3E SR to SM under different SMAP-h values. The sensitivity of GNOS-II SR to SM is in general agreement with the values in the previous studies, demonstrating the feasibility of using single-pass multi-GNSS constellation GNSS-R data to retrieve surface parameters, such as SM, with shorter revisit times. Furthermore, the results of this study re-emphasize the nonlinear sensitivity of SR to SM. As compared with higher SM, SR is more sensitive at lower SM. This highlights the shortcomings of using linear models to retrieve SM. Meanwhile, another important finding is that, for spaceborne GNSS-R data, SMAP-h may have underestimated the effective surface roughness.**

***Index Terms*—Fengyun-3E (FY-3E), global navigation satellite system reflectometry (GNSS-R), soil moisture (SM), surface reflectivity (SR), surface roughness, vegetation.**

Received 5 July 2024; revised 23 September 2024; accepted 31 October 2024. Date of publication 11 November 2024; date of current version 27 November 2024. The work of Zhongmin Ma was supported by China Scholarship Council (CSC) through a State Scholarship Fund under Grant 202306560073. This work was supported in part by the National Natural Science Foundation of China Projects under Grant 42074041; in part by Shaanxi Province Science and Technology Innovation Team under Grant 2021TD-51; in part by the Innovation Team of Shaanxi Provincial Tri-Qin Scholars with Geoscience Big Data and Geohazard Prevention (2022); in part by the Fundamental Research Funds for the Central Universities under Grant CHD300102263715; and in part by the Project "GENESIS: GNSS Environmental and Societal Missions – Subproject UPC," under Grant PID2021-126436OB-C21 funded by the Ministerio de Ciencia e Investigación (MCIN)/Agencia Estatal de Investigación (AEI)/10.13039/501100011033 and EU FEDER "Una Manera de Hacer Europa." *(Corresponding author: Zhongmin Ma.)*

Zhongmin Ma is with the College of Geological Engineering and Geomatics, Chang'an University, Xi'an 710054, China, and also with the CommSensLab – UPC, Universitat Politècnica de Catalunya – BarcelonaTech, 08034 Barcelona, Spain (e-mail: zhongminma@chd.edu.cn).

Adriano Camps is with the CommSensLab – UPC, Universitat Politècnica de Catalunya – BarcelonaTech, 08034 Barcelona, Spain, also with the Institut d'Estudis Espacials de Catalunya (IEEC) – CTE-UPC, E-08034 Barcelona, Spain, and also with UAE University, Al-Ain 15551, UAE (e-mail: adriano.jose.camps@upc.edu).

Hyuk Park is with the CommSensLab – UPC, Universitat Politècnica de Catalunya – BarcelonaTech, 08034 Barcelona, Spain, and also with the Institut d'Estudis Espacials de Catalunya (IEEC) – CTE-UPC, E-08034 Barcelona, Spain (e-mail: park.hyuk@upc.edu).

Shuangcheng Zhang is with the College of Geological Engineering and Geomatics, Chang'an University, Xi'an 710054, China (e-mail: shuangcheng369@chd.edu.cn).

Xiaojun Li and Jean-Pierre Wigneron are with the INRAE, UMR1391 ISPA, Université de Bordeaux, F-33140 Villenave d'Ornon, France (e-mail: xiaojun.li@inrae.fr; jean-pierre.wigneron@inrae.fr).

Digital Object Identifier 10.1109/JSTARS.2024.3496313

I. Introduction

In 1988, the concept of using the reflected signals of the global positioning system (GPS) as signals of opportunity to achieve multistatic scattering measurements was first proposed [1]. Subsequently, in 1991, an incident in a French aircraft testing a GPS receiver demonstrated for the first time that GPS signals scattered from the sea surface could be acquired and tracked [2]. In 1993, the European Space Agency introduced the concept of what it is called today interferometric global navigation satellite system reflectometry based on the cross correlation of the direct and reflected signals for mesoscale ocean altimetry [3]. In 1996, NASA proposed what is called today conventional GNSS-R based on the cross correlation of the scattered signal with a locally generated copy of the direct signal [4]. In 1997, NASA first collected GPS-reflected signals during an airborne experiment [5], and in 2002, the first GPS-R data from space were found in SIR-C data [6]. In September 2003, the U.K. launched the first spaceborne GNSS-R payload demonstrator on board the U.K.-DMC [7]. Then, in July 2014, the U.K. also successfully launched the TechDemoSat-1 mission (TDS-1) with an improved GNSS-R payload (SGR-ReSI) [8]. A

TABLE I
CHARACTERISTICS OF DIFFERENT GNSS SIGNALS RECEIVED BY FY-3E GNOS-2

	GPS L1 C/A	BDS B1I	GAL E1B
Frequency (MHz)	1575.42	1561.098	1575.42
Modulation	BPSK	BPSK	BOC (1,1)
Chipping rate (Mcps)	1.023	2.046	2.046
Code length (ms)	1	1	4

series of studies using U.K.-DMC and TDS-1 data demonstrated the feasibility of GNSS-R for ocean, land, and ice measurements [9], [10], [11]. In the following ten years, a number of other small satellites with GNSS-R payloads were successfully launched. These include NASAs cyclone global navigation satellite system (CYGNSS) [12], the ^{3}Cat series of CubeSats led by the NanoSat Lab of the Universitat Politècnica de Catalunya [13], [14], and the BuFeng-1 A/B of the China Aerospace Science and Technology Corporation [15]. The increase in available scientific data has advanced the development of spaceborne GNSS-R technology. In addition to the initial sea surface applications [16], [17], extensive literature has demonstrated the potential of spaceborne GNSS-R to retrieve soil moisture (SM) [10], [18], [19], [20], [21], vegetation [22], [23], inland water bodies [24], [25], [26], flooding [27], [28], [29], as well as surface freezing and thawing [30], [31], [32]. Although many GNSS-R studies have been reported in the literature, there are very few using BeiDou (BDS) and Galileo (GAL), mostly using data recorded in the CYGNSS raw intermediate frequency (raw IF) data [33], [34].

In July 2021, China successfully launched Fengyun-3E (FY-3E), with the global navigation satellite occultation sounder-II (GNOS-II), which can simultaneously receive reflected signals from GPS, BDS, and GAL. Through multiconstellation measurements, it significantly reduces the revisit time of the spaceborne GNSS-R data. Using the GNSS-R data provided by FY-3E, this study investigated the similarities and differences in the sensitivity of the reflected signals from multi-GNSS constellations to land surface parameters at different incidence angles. Vegetation effects were also accounted for through a two-way attenuation model using the soil moisture and ocean salinity (SMOS) INRA-CESBIO (SMOS-IC) *L*-band vegetation optical depth (L-VOD).

The rest of this article is organized as follows. Section II briefly describes the FY-3E satellite mission with its GNSS-R data characteristics and introduces the other data used in this article. Section III presents the methodology to calculate the FY-3E GNOS-II surface reflectivity (SR) and the calibration to vegetation effects. Section IV describes the sensitivity of the FY-3E SR to SM and SMAP-h parameter under different conditions and compares in detail the results of this study with the ones in the published literature. Finally, Section V concludes this article.

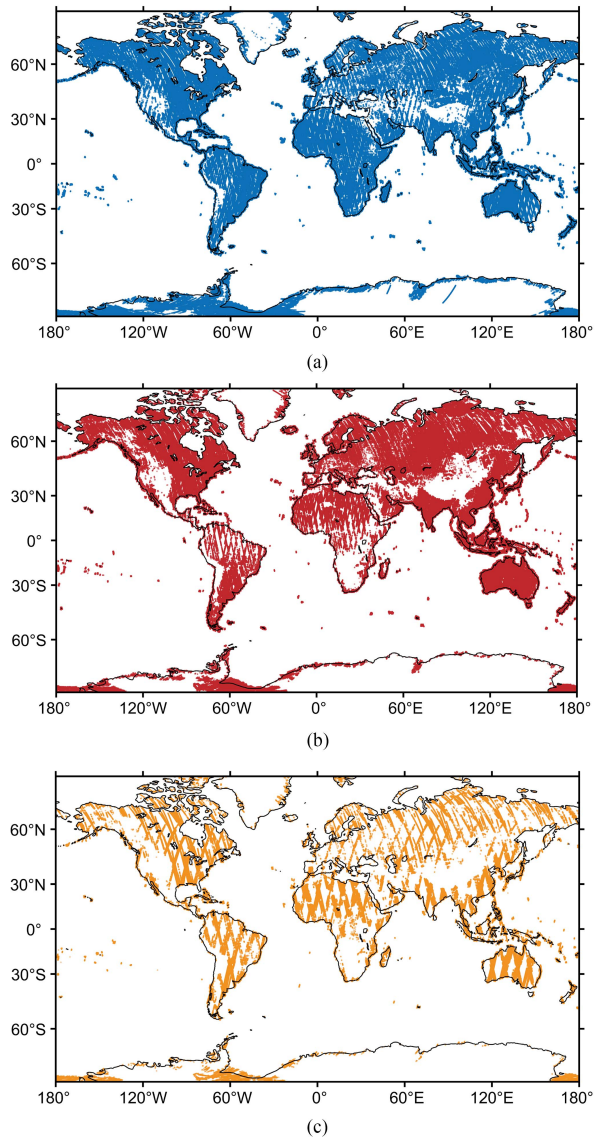

Fig. 1. Distribution of GNOS-II GNSS-R observations in May 2023 after quality control. (a) GPS. (b) BDS. (c) GAL.

II. MATERIALS

A. Fengyun-3E

FY-3E is a Chinese second-generation meteorological satellite and the 19th satellite in the Feng Yun series of meteorological satellites [35]. FY-3E is located in a sun-synchronous polar orbit with an orbital altitude of 836 km, and an inclination of 98.75° [36]. FY-3E provides ionospheric electron density information, atmospheric refractive index, atmospheric temperature, and humidity information over a latitude range of 85° North to South. In addition, the FY-3E carries an upgraded version of the GNOS-II payload that provides both GNSS radio occultations (GNSS-RO) and reflectometry (GNSS-R). The GNOS-II is equipped with two upward zenith pointing antennas for positioning, two side-pointing antennas for GNSS-RO, and a nadir-looking antenna for GNSS-R [36]. It has eight

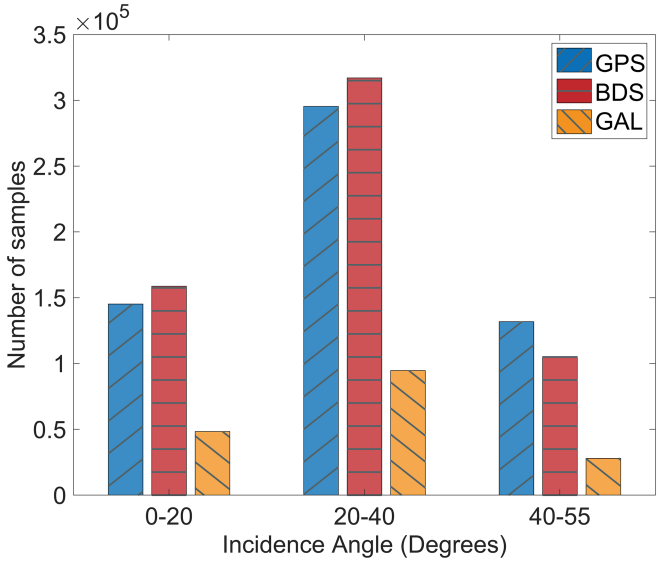

Fig. 2. Histogram of GPS, BDS, and GAL GNOS-II GNSS-R observations under different incidence angles (May 2023).

channels to track reflected signals, enabling it to receive signals from eight different navigation satellites simultaneously.

In July 2022, by switching some of the BDS channels to GAL channels, the FY-3E achieved operational acquisition of reflected GPS, BDS, and GAL signals. Besides, it has a global data latency of less than 3 h, which makes it suitable for applications, such as data assimilation in operational numerical weather prediction models and tropical cyclone monitoring. Currently, GNOS-II is measuring the signals of GPS L1 C/A, BDS B1I, and GAL E1B. Table I gives detailed information about these three signals.

As with other spaceborne GNSS-R missions, the fundamental observables for FY-3E GNOS-II are the delay Doppler maps (DDMs). DDMs are calculated by cross correlating the received signal with a Doppler frequency-shifted replica of the transmitted GNSS signal locally generated by the receiver, with 1 ms coherent, and 1 s incoherent integration times. The nominal sampling frequency of GNOS-II DDM is 1 Hz. Unlike CYGNSS, the DDMs generated by FY-3E GNOS-II are in a nonuniform grid, and their size is 122 delay × 20 Doppler bins, where 1/8 chip delay interval is used for the delay of the [−3, 2.875] chips around the specular reflection point, and 1/4 chip interval is used for the rest of the delay range [36]. A nonuniform DDM allows for a denser sampling around the specular point. GNOS-II L1 data spanning from May 2023 to October 2023 is used in this article [37]. In addition to the DDMs, ancillary data, such as the latitude and longitude of the specular point, the location of the receiver and transmitter, the DDM sampling time, and the quality labels are also included in the L1 data. To ensure the reliability of the results, data with receiver antenna gain less than 0 dB or signal-to-noise ratio (SNR) less than −4 dB were removed from this study.

The distribution of GNSS-R observations in May 2023 for the different GNSS constellations of GNOS-II is shown in Fig. 1. Although GPS, BDS, and GAL observations all provide global coverage, GAL has significantly fewer observations than GPS and BDS. Further statistics on the number of reflection points sampled in May 2023 for GNOS-II GPS, BDS, and GAL are shown in Fig. 2.

The results in Fig. 2 show that the number of sampling points for GAL is about one-third of that for GPS and BDS for all ranges of incidence angles. This is caused by the different assignments of the GNOS-II-reflected signal channels. Besides, the number

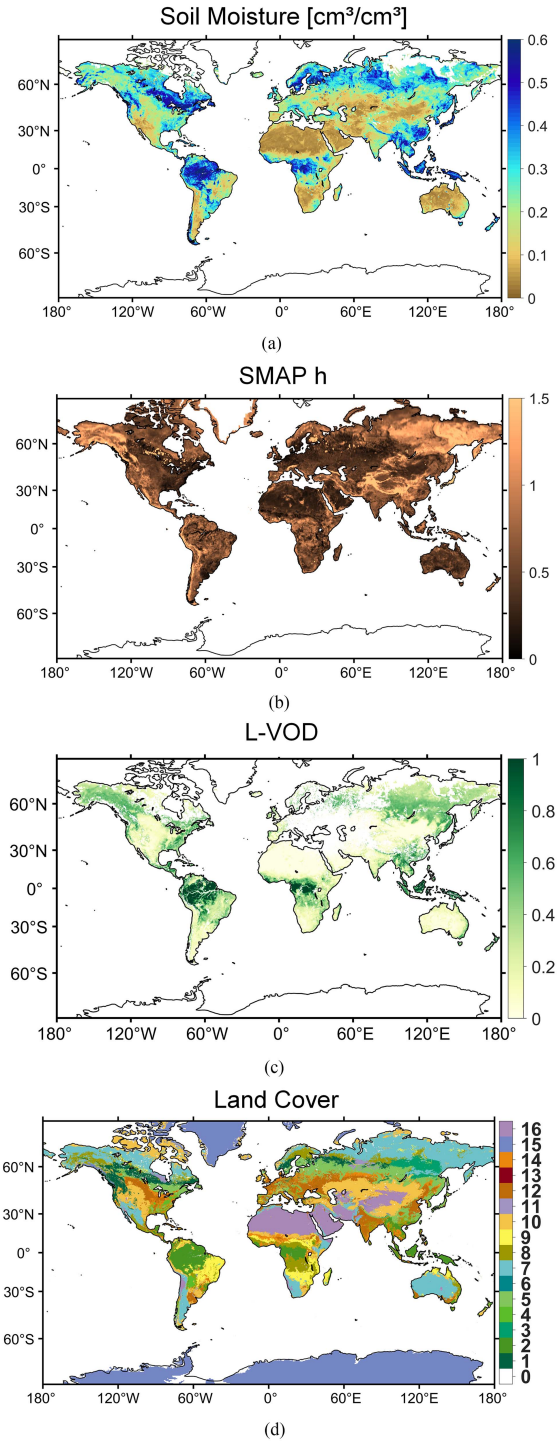

Fig. 3. Auxiliary data used in this article. (a) May 2023 global mean SM (obtained from SMAP). (b) Global surface roughness (obtained from SMAP-h). (c) May 2023 global mean L-VOD (obtained from SMOS-IC). (d) IGBP LC (9∗9 km EASE grid cell), data from SMAP ancillary data.

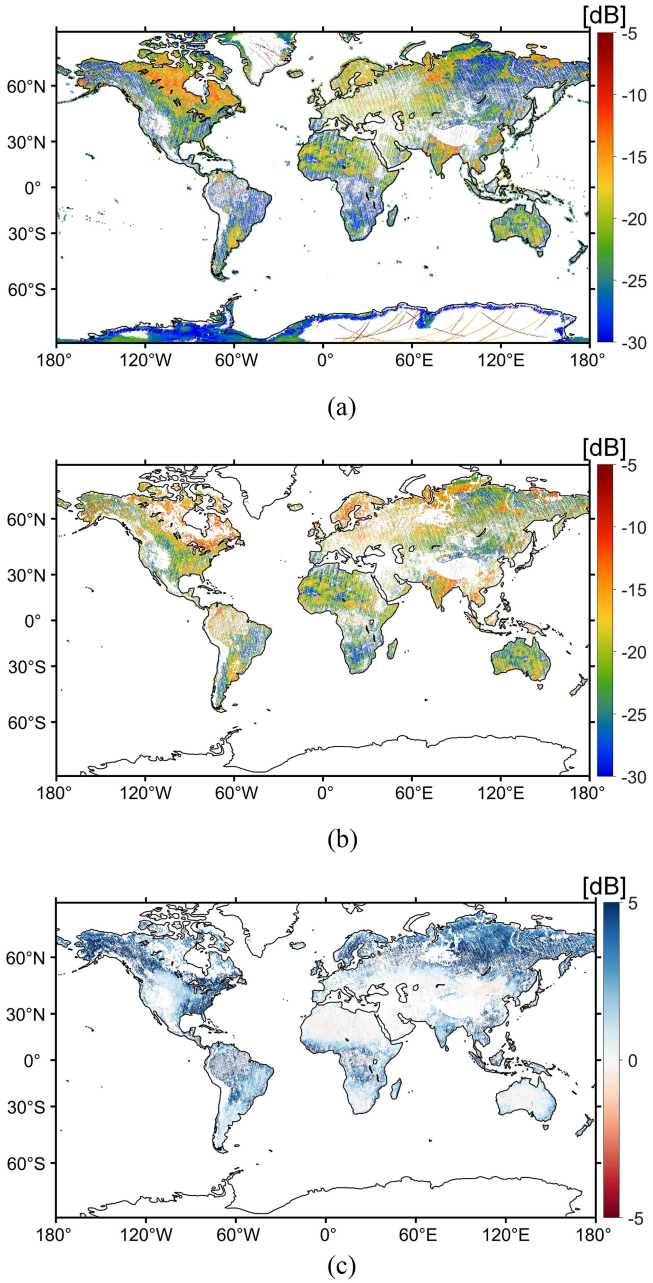

Fig. 4. SR retrieved from GNOS-II. (a) GPS SR before vegetation correction (May 2023). (b) GPS SR after vegetation correction (May 2023). (c) Changes before and after correction (correction − noncorrection).

of observation samples in the 20°–40° range is significantly larger than the other two angular ranges. It should also be noted that the incidence angle of the GNOS-II-reflected signals is up to about 55° [38].

B. Soil Moisture Active Passive (SMAP) SM

NASA SMAP mission was launched in 2015. It consists of an *L*-band radiometer (passive) and a radar (active). After the radar failure, only radiometer data are provided [39]. SMAP has a revisit time of about 2–3 days, and it can provide near-global coverage of SM and freeze−thaw status products. In this article, the SMAP L3 daily global SM product is used, which

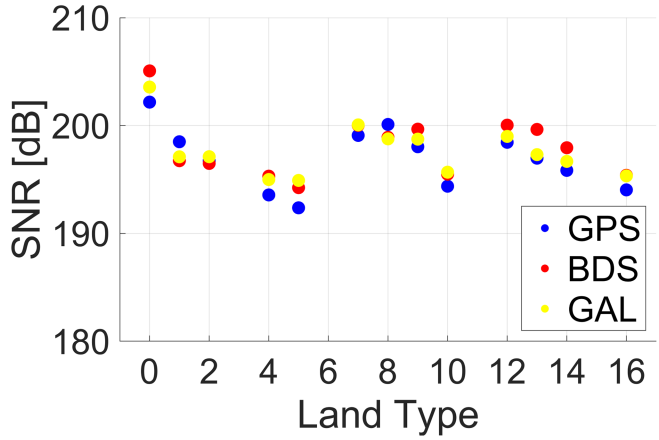

Fig. 5. Scatter plot for SNR of reflected signals from GPS (blue), BDS (red), and GAL (yellow) on 17 LCs. The *X*-axis in the graph represents LC with corresponding numbers [see Fig. 3(d)].

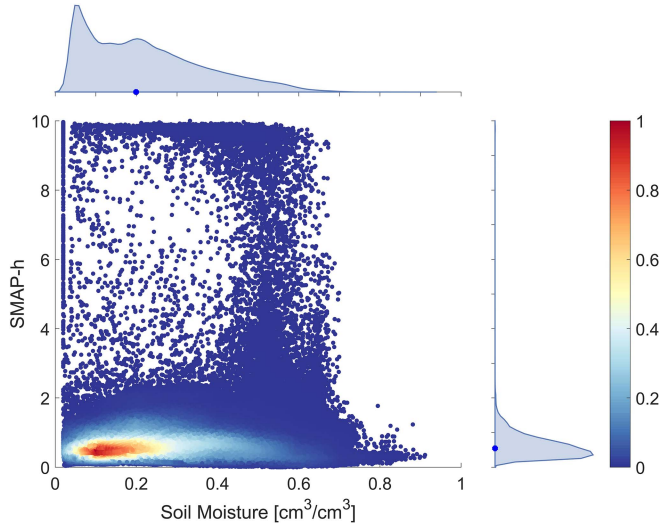

Fig. 6. Density scatter plot and pdf distribution of global SMAP SM versus corresponding SMAP-h for May 2023. The blue circle on the pdf distribution represents the median of the data.

is provided in an EASE-Grid 2.09 km grid [40]. To obtain a more complete spatial coverage, both ascending and descending orbit measurements are used. The data span from May 2023 to October 2023. Fig. 3(a) gives the SMAP global average SM in May 2023.

C. Surface Roughness

Besides SM, surface roughness is also an important factor affecting the SR. In this study, the surface roughness data from SMAP (SMAP-h) provided in the SMAP static auxiliary dataset is selected to investigate the sensitivity of SR to SM under different surface roughness [41]. In many studies that use spaceborne GNSS-R to retrieve SM, SMAP-h is also a common auxiliary data used to remove the surface roughness effect. This product is also offered in an EASE-Grid 2.09 km grid. SMAP-h is a unitless value derived from the land cover (LC) type to characterize the surface roughness of bare soil [42]. However, it should be noted that some works have pointed out that SMAP-h may underestimate the true surface roughness in some areas

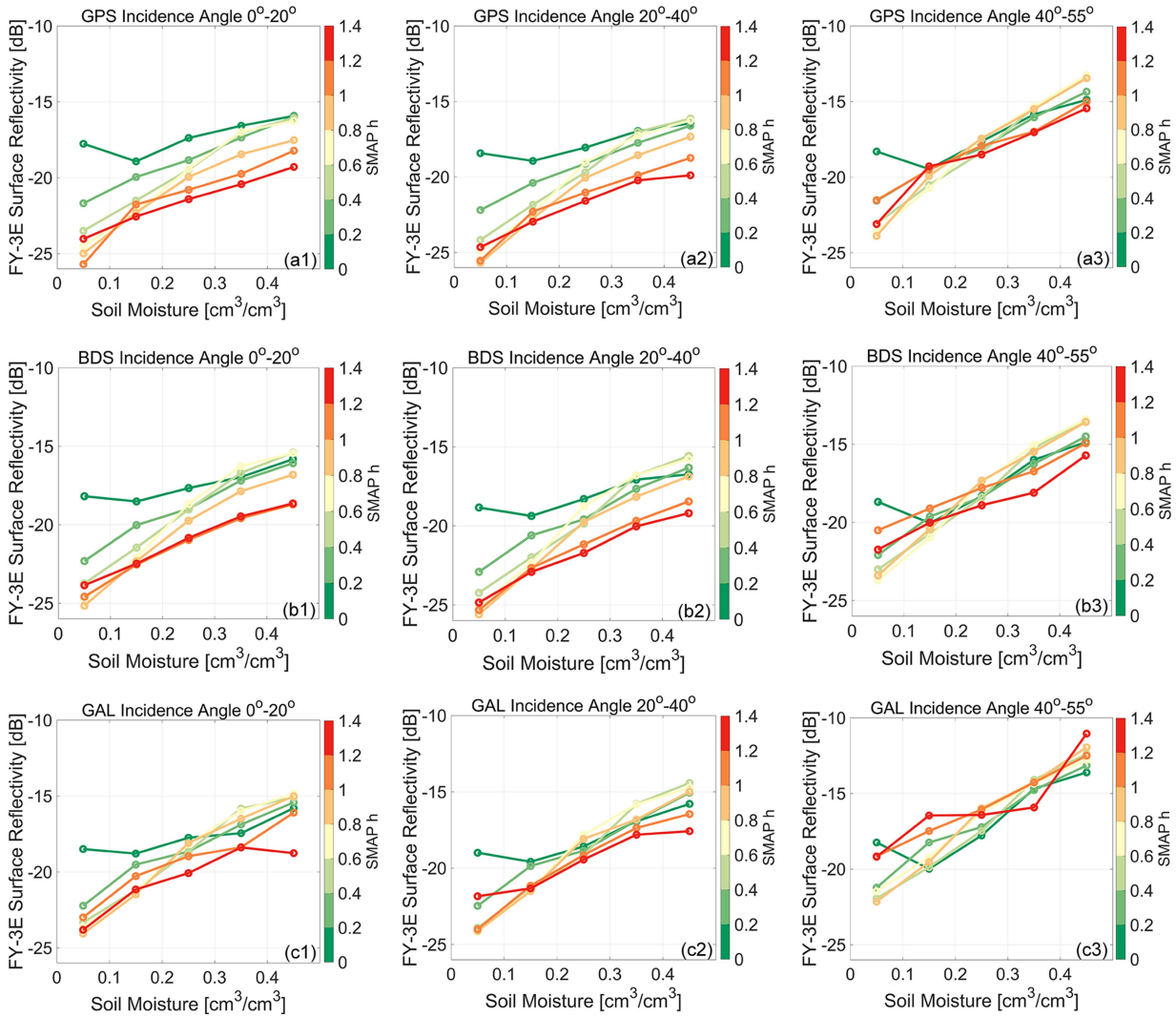

Fig. 7. Sensitivity of GNOS-II SR to SM for different incidence angles and different surface roughness (SMAP-h). (a1)–(a3) GPS. (b1)–(b3) BDS. (c1)–(c3) GAL.

[43], [44], [45], and that surface roughness may also change with SM [46]. At the same time, it should be reminded that there is currently no uniformly recognized effective surface roughness parameter applicable to microwave remote sensing. In addition, there are several surface roughness measurement methods, but the surface roughness measured by different measurement methods is different. Some studies have pointed out that even surface roughness measured in the field may not be suitable for GNSS-R measurements [47]. Fig. 3(b) illustrates the global distribution of the SMAP-h.

D. SMOS-IC L-VOD

Vegetation attenuates microwave signals, and denser vegetation also causes larger volume scattering. In this article, the SMOS-IC L-VOD data are used to remove the vegetation effects in GNOS-II SR by means of a two-way attenuation model [48], [49], [50], [51], [52]. After that, the sensitivity of GNOS-II SR to SM and surface roughness will be analyzed. The SMOS-IC L-VOD is provided in an EASE-Grid 2.025 km grid, and in this article, it is regridded to an EASE-Grid 2.09 km grid. The L-VOD data used in this article span from May 2023 to October 2023. Fig. 3(c) shows the global average SMOS-IC L-VOD in May 2023.

E. International Geosphere–Biosphere Program (IGBP) LC

In order to compare the SNR quality of GNSS-R measurements from different GNSS constellations (GPS, BDS, and GAL), here we introduce another auxiliary data, LC. As with the sources of auxiliary data used in our article, LC data are used from ancillary data of SMAP product, derived from the moderate resolution imaging spectroradiometer IGBP LC. The primary LC scheme identifies 17 classes defined by the IGBP, including: 0: water bodies; 1: evergreen needleleaf forest; 2: evergreen broadleaf forest; 3: deciduous needleleaf forest; 4: deciduous broadleaf forest; 5: mixed forest; 6: closed shrublands; 7: open shrublands; 8: woody savannas; 9: savannas; 10: grasslands; 11: permanent wetlands; 12: croplands; 13: urban and built-up; 14: cropland/natural vegetation mosaic; 15: permanent snow and ice; and 16: barren or sparsely vegetated. Fig. 3(d) presents the IGBP LC.

TABLE II
SLOPE OF LINEAR FIT OF GNOS-II GPS SR TO SM UNDER DIFFERENT INCIDENCE ANGLES AND DIFFERENT SURFACE ROUGHNESS (SMAP-H)

GPS		0<h<0.2	0.2<h<0.4	0.4<h<0.6	0.6<h<0.8	0.8<h<1	1<h<1.2	1.2<h<1.4
Incidence angle 0°–20°	0< SM<0.2	**–11.61**	17.3	19.86	22.28	26.86	39.39	14.7
	0.2< SM<0.45	7.28	14.32	16.95	15.82	12.11	12.91	10.62
	0< SM<0.45	6.02	14.02	19.32	21.8	18.77	16.98	11.61
Incidence angle 20°–40°	0< SM<0.2	**–5.1**	18.01	23.37	25.22	29.63	32.49	16.85
	0.2< SM<0.45	7.8	12.55	17.81	13.96	13.62	11.45	8.45
	0< SM<0.45	5.91	13.83	20.9	22.42	20.89	16.01	12.26
Incidence angle 40°–55°	0< SM<0.2	**–11.6**	20.74	25.59	28.84	39.58	20.18	38.16
	0.2< SM<0.45	13.73	18.64	24.63	21.08	19.97	14.58	15.26
	0< SM<0.45	10.45	17.87	24.4	26.09	25.28	15.53	17.56

Negative sensitivities are highlighted in bold.

TABLE III
SLOPE OF LINEAR FIT OF GNOS-II BDS SR TO SM UNDER DIFFERENT INCIDENCE ANGLES AND DIFFERENT SURFACE ROUGHNESS (SMAP-H)

BDS		0<h<0.2	0.2<h<0.4	0.4<h<0.6	0.6<h<0.8	0.8<h<1	1<h<1.2	1.2<h<1.4
Incidence angle 0°–20°	0<SM<0.2	**–3.32**	22.89	22.86	27.03	28.3	20.54	13.71
	0.2<SM<0.45	9.19	14.49	18.1	16.18	14.61	11.32	10.98
	0<SM<0.45	6.26	15.31	21.43	24.54	21.14	14.72	13.43
Incidence angle 20°–40°	0<SM<0.2	**–5.35**	23.09	22.49	27.13	28.74	26.62	19.36
	0.2<SM<0.45	7.81	16.35	21.39	14.99	14.4	13.57	12.6
	0<SM<0.45	6.5	16.14	22.5	24.15	22.02	16.71	14.19
Incidence angle 40°–55°	0<SM<0.2	**–13.55**	24.59	22.79	27.4	29.81	13.91	17.27
	0.2<SM<0.45	17.2	19.38	24.67	20.21	18.83	14.3	15.94
	0<SM<0.45	11.69	18.54	24.59	26.48	24.59	13.52	13.97

Negative sensitivities are highlighted in bold.

TABLE IV
SLOPE OF LINEAR FIT OF GNOS-II GAL SR TO SM UNDER DIFFERENT INCIDENCE ANGLES AND DIFFERENT SURFACE ROUGHNESS (SMAP-H)

GAL		0<h<0.2	0.2<h<0.4	0.4<h<0.6	0.6<h<0.8	0.8<h<1	1<h<1.2	1.2<h<1.4
Incidence angle 0°–20°	0< SM<0.2	**–2.98**	27.12	21.3	23.17	25.75	27.16	26.62
	0.2< SM<0.45	9.75	16.17	17.86	16.56	15.39	14.34	6.57
	0< SM<0.45	6.73	16.25	21.83	22.79	23.08	15.69	12.87
Incidence angle 20°–40°	0< SM<0.2	**–5.89**	26.08	25.4	27.45	26.18	28.4	5.15
	0.2< SM<0.45	13.94	19.03	23.58	15.56	15.48	13.4	9.3
	0< SM<0.45	9.05	17.82	24.53	24.51	22.94	18.87	12.04
Incidence angle 40°–55°	0< SM<0.2	**–17.43**	29.87	20.62	22.43	26.24	16.7	27.26
	0.2< SM<0.45	20.84	20.34	25.49	17.34	20.14	17.81	26.87
	0< SM<0.45	14.56	19.6	24.9	22.23	25.7	16.52	16.81

Negative sensitivities are highlighted in bold.

III. METHODS

A. FY-3E GNOS-II SR

Currently, most studies using spaceborne GNSS-R observations to retrieve surface parameters use either the SNR or the SR derived from the DDMs. The sensitivity of *L*-band microwave signals to the surface dielectric constant is utilized to monitor changes in SM or to detect inland water bodies and freeze−thaw status. In addition, some studies have also used the power ratio method based on the DDM shape or waveform [53], [54], [55]. However, most studies assume that the surface reflection signal is dominated by the coherent components and ignore the influence of the incoherent components. This article follows this assumption and uses the following equation to obtain the GNOS-II SR [56], [57]:

$$\Gamma(\theta) = \frac{(R_t + R_r)^2 P_{\mathrm{DDM}}}{F R_t^2 R_r^2 4\pi} \tag{1}$$

where θ is the incidence angle, $\Gamma(\theta)$ is the SR, R_t and R_r are the distances from the GNSS satellite and GNOS-II to the specular reflection point, respectively, P_{DDM} is the DDM peak power, and F is the so-called DDM bistatic radar cross-sectional factor [38], [58], which is defined as follows:

$$F = \frac{\lambda^2 P_t G_t G_r}{(4\pi)^3 R_t^2 R_r^2} \tag{2}$$

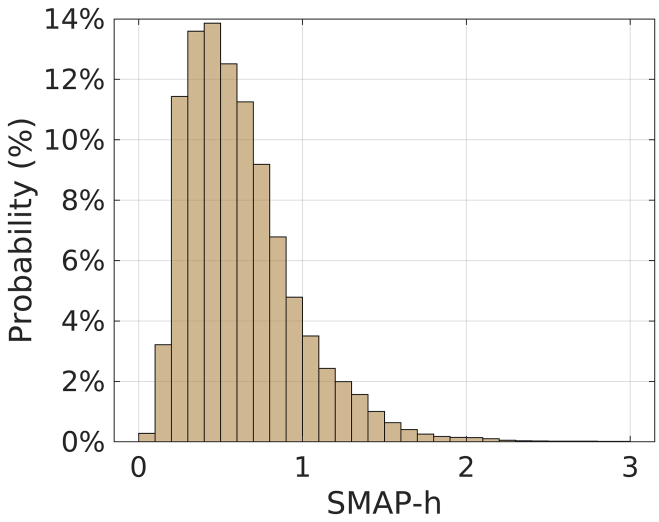

Fig. 8. SMAP-h statistical chart.

where λ is the wavelength of the GNSS signal (0.1903 m for GPS and GAL, and 0.1921 m for BDS), $P_t G_t$ is the GNSS effective isotropic radiated power, and G_r is the receiver antenna gain. The value of F is included in the FY-3E GNOS-II L1 data. Through these two equations, the GNOS-II SR can be obtained for different GNSS constellations.

B. Vegetation Effect Calibration

To remove the effect of vegetation in the reflected signal, a two-way extinction model (where extinction includes both attenuation and scattering effects) widely used in microwave remote sensing was used to obtain the SR of bare soil ($\Gamma_{\text{soil}}(\theta)$) [47], [59]

$$\Gamma_{\text{soil}}(\theta) = \Gamma(\theta) \cdot \exp(2 \cdot \tau / \cos\theta) \tag{3}$$

where θ is the incidence angle, and τ is the L-VOD. Through (3), the observed reflectivity can be corrected to the reflectivity of the soil surface. The GNOS-II GPS SR and its changes before and after vegetation correction in May 2023 are given in Fig. 4. In most areas around the world, the two-way attenuation model combined with L-VOD compensates well for the signal attenuation caused by vegetation absorption. Of these, the denser the vegetation, the larger the compensation. However, it should be noted that a slight overcompensation occurs in a few areas with almost no vegetation cover (e.g., Sahara Desert and Mongolian Plateau). This suggests that in the few areas where vegetation is sparse, further assessment of the potential of L-VOD to estimate vegetation is needed.

IV. Results and Discussion

A. Comparison of SNR for Different GNSS Constellations

In order to compare the quality of SNR from different GNSS constellations, the SNR data of different GNSS constellations provided by FY-3E are first gridded to 9∗9 km, and the value of each grid is equal to the average of all SNRs falling into the grid. The FY-3E data used are from May 2023. Afterward, we compare the performance of SNR for different GNSS constellations and GNSS-R measurements under different LCs.

In the process of statistics, the LC with a number of observations less than 2% of the total number of observations was deleted in order to ensure the reliability of statistics. As it can be seen in Fig. 5, the SNR values of the reflected signals from different GNSS constellations are close to each other for all LCs. The SNR of GPS, BDS, and GAL varies about 0–3 dB for different LCs. This indicates that the quality of SNR is similar for different GNSS constellations and GNSS-R measurements. Besides, by observing Fig. 5, it can be noticed that the water body corresponds to the maximum SNR value, while deciduous broadleaf forest and mixed forest correspond to the minimum SNR value. This finding is consistent with that previously reported in the literature [34].

B. Distribution of SMAP SM and SMAP-h

Fig. 6 presents a density scatter plot and probability density function (pdf) distributions of global SMAP SM and the corresponding SMAP-h for May 2023. Studies of data from other months yielded similar results and are not shown. As it can be noticed from Fig. 6, SM is mainly distributed between 0 and 0.5 cm³/cm³, while SMAP-h is mainly concentrated between 0 and 1.5.

To explore the changes in sensitivity of the GNOS-II SR to SM under different SMAP-h values, we further grouped the data in steps of $\Delta\text{SM} = 0.1$ and $\Delta\text{SMAP-h} = 0.2$.

C. Sensitivity of GNOS-II SR to SM and SMAP-h

Fig. 7 shows the GPS, BDS, and GAL-calibrated SR for different SMs under different incidence angles and different surface roughness (SMAP-h).

As it can be seen in Fig. 7, the SR of GPS, BDS, and GAL increases with SM with an approximate linear trend, for all incidence angles, and all surface roughness. This is consistent with many publications that have used a linear fit to retrieve SM from spaceborne GNSS-R data [18], [19], [20]. Further investigations show that when the incidence angle is less than 40°, the increase in SR at lower surface roughness ($0 <$ SMAP-h < 0.2) is smaller than that at higher surface roughness.

Further observations revealed that the GNOS-II SR exhibited different sensitivities to different SMs within the entire SM interval. Specifically, SR is more sensitive to SM when SM $<$ 0.2 cm³/cm³ and shows a stronger tilt, which is more pronounced at incidence angles less than 40°. This pattern is consistent with the description of the nonlinear increasing relationship between SR and SM in the published literature [44], [47], [60], [61], [62], [63], [64], [65]. When the incidence angle is higher than 40°, the above pattern is no longer obvious, but the SR under each SMAP-h becomes more concentrated, indicating that the effect of surface roughness on SR becomes smaller at this time. This phenomenon has also been reported in the previous literature [66], and it can be due to the effect of the incidence angle (θ).

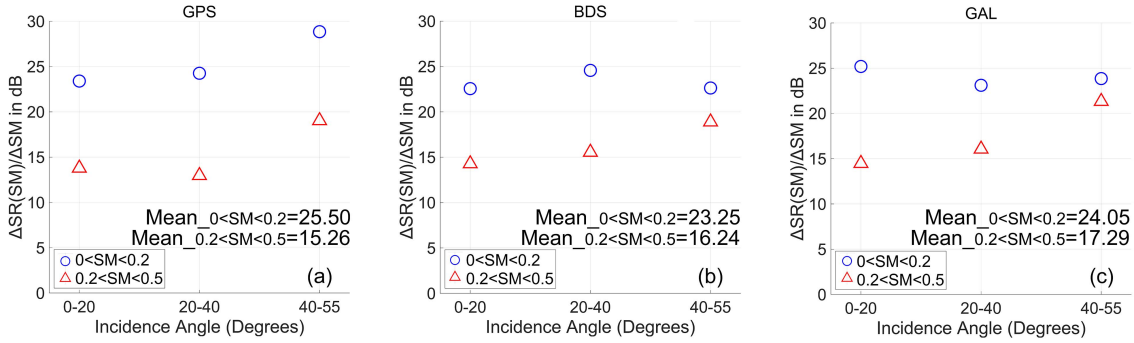

Fig. 9. Average slope of the linear fit of GNOS-II SR to SM when SMAP-h > 0.2. (a) GPS. (b) BDS. (c) GAL.

According to the Rayleigh roughness criterion [67]

$$h < \frac{\lambda}{8\cos\theta} \tag{4}$$

where λ is the wavelength of the incident signal, and θ is the incidence angle, even a rough surface can be considered to be a smooth surface for large incidence angles.

Linear fit was further performed in the data grouped according to surface roughness (SMAP-h) to quantitatively analyze changes in sensitivity. Tables I–IV give the slopes of the linear fit of SR to SM for different groupings.

As it can be seen from Tables I–IV, the sensitivity ($(\Delta\mathrm{SR}/\Delta\mathrm{SM})$ [dB]) of GNOS-II SR to SM of $0 < \mathrm{SM} < 0.2$ is much higher than that to SM of $0.2 < \mathrm{SM} < 0.45$ for all GNSS constellations, except for $0 <$ SMAP-h < 0.2. It should be noted that some studies indicate that soil may be saturated when SM is equal to 0.4–0.45 [68]. Besides, a negative sensitivity behavior is also observed in the $0 <$ SMAP-h < 0.2 subgroup (shown in bold type in the tables). The reasons for this phenomenon will be discussed in detail afterward. Specifically, when the incidence angle is 0°–20° and $h > 0.2$, the sensitivities of GPS, BDS, and GAL to $0 < \mathrm{SM} < 0.2$ are 23.40, 22.56, and 25.19, respectively (these values are very close to the simulation results in [60]); however, for $0.2 < \mathrm{SM} < 0.45$, the sensitivities drop to 13.79, 14.28, and 14.48, respectively. For the entire SM interval ($0 < \mathrm{SM} < 0.45$), the sensitivities are 17.08 (GPS), 18.43 (BDS), and 18.75 (GAL). Although the sensitivity of GNOS-II SR to SM in the range $0 < \mathrm{SM} < 0.45$ was slightly higher than to SM in the range $0.2 < \mathrm{SM} < 0.45$, it was still significantly lower than to SM in the range $0 < \mathrm{SM} < 0.2$. The results of the quantitative analyses validate previous speculations that GNSS-R SR is more sensitive to low SM.

At the same time, it should be pointed out that results obtained for $0 < h < 0.2$ have led to very different conclusions. Specifically, GNOS-II SR seems to be more sensitive to $0.2 < \mathrm{SM} < 0.45$ than to $0 < \mathrm{SM} < 0.2$. In addition, some negative sensitivity was also observed in the $0 < h < 0.2$ and $0 < \mathrm{SM} < 0.2$ subgroup, i.e., as SM increases, SR decreases (bold font in Tables I–IV). To the best knowledge of the authors of this article, this phenomenon has not been reported before in the published literature. One possible reason is that SMAP-h may not be a good representation of the actual effective surface roughness for spaceborne GNSS-R. Another possible reason is the uncertainty in SMAPs estimation of low SM ($0 < \mathrm{SM} < 0.2$). Fig. 8 shows the statistical graph of SMAP-h. It can be seen that 95% of the SMAP-h are less than 1.5. Of these, less than 4% of SMAP-h fall into the 0–0.2. There have been reports in the literature that the SMAP-h may be underestimating the actual effective surface roughness [43], [44], [45]. Subsequent studies need to further discuss the sensitivity of GNSS-R SR to SM at low SMAP-h. More importantly, an in-depth analysis of the reliability of using SMAP-h as a surface roughness parameter for spaceborne GNSS-R data is also necessary.

Furthermore, in some subgroups, the behavior of increasing sensitivity with increasing incidence angle can be observed. There is currently no reasonable explanation for this phenomenon. One possible reason remains that SMAP-h is not applicable to spaceborne GNSS-R data. Another possible reason is that, at 40°–55°, the signal has a shorter path through the vegetation, making it more sensitive to the soil. In addition, it is possible that the angular range of that observation is close to SMAPs incidence angle of 40°, while the SM data used in this article are from SMAP. However, according to the previous studies, within the incident angle range of 0°–55°, the sensitivity of SR to SM does not change significantly with the incident angle [44]. This highlights the importance of further investigating the variation in SR sensitivity to SM (or other Earth surface parameters, e.g., vegetation) at different incidence angles and different surface roughness.

In addition, when $0.2 <$ SMAP-h < 1, for all SMs and all incidence angles, the sensitivities of GPS, BDS, and GAL to SM are 20.62, 21.17, and 21.53, respectively. However, when SMAP-h > 1, the sensitivity dropped to 14.56, 11.13, and 18.07, respectively. The sensitivity of GNOS-II SR to SM decreases as the surface roughness (SMAP-h) increases. Moreover, by observing Fig. 7, it can also be noticed that GAL seems to be less sensitive to SMAP-h than GPS and BDS when the incidence angle is less than 40°. Possible reasons for this are the different modulation and longer code period of the GAL, 4 ms, instead of 1 ms as in GPS and BDS. Considering that surface roughness is a major error source affecting the retrieval of surface parameters by spaceborne GNSS-R, future work should study this phenomenon in more depth.

To make our results clearer, Fig. 9 shows the average slope of the linear fit of GNOS-II SR to SM when SMAP-h > 0.2.

The results in Fig. 9 again illustrate that GNOS-II SR is more sensitive to SM when $0 < \mathrm{SM} < 0.2$. A comparison of the results in Fig. 9 also shows that the sensitivity of the GNOS-II SR to

SM does not change much for different GNSS constellations and different incidence angles. Possible reasons for this are that the signals currently collected by GNOS-II are very similar in frequency and the maximum incidence angle of the reflected signals is only about 55°.

V. Conclusion

The main research objective of this work is the analysis of the sensitivity of the reflected signals from different GNSS constellations of the FY-3E GNOS-II to SM and surface roughness. The effect of vegetation was first corrected using the two-way attenuation model and the SMOS-IC L-VOD. An overcorrection was found in some areas with sparse vegetation (e.g., Sahara, Mongolia). Then, the sensitivity of the bare soil SR to SM under different SMAP-h was analyzed. Quantitative statistics show that the sensitivity of GNOS-II SR to SM is nonlinear. SR is more sensitive to lower SM ($0 < \text{SM} < 0.2$) than to higher SM ($0.2 < \text{SM} < 0.45$). As SM increases, the sensitivity of SR to SM decreases. This is consistent with the results of simulations in the previous studies. Moreover, the sensitivity of GNOS-II SR to SM decreases as the surface roughness (SMAP-h) increases. At the same time, it was also observed that, at high incident angles, the effect of surface roughness (SMAP-h) on GNOS-II SR is weakened. This very interesting effect could be used to limit the effect of roughness on GNSS-R SM retrievals. In addition, the sensitivity of GNOS-II SR to SM is similar for the three different GNSS constellations and different incidence angles, despite their different code lengths and chipping rates.

It is noteworthy that the studies of the $0 < h < 0.2$ subgroup reached the opposite conclusion to the above results. The possible reason for this is the underestimation of the actual effective surface roughness by SMAP-h. This indicates the necessity to further investigate the reliability of using SMAP-h as the surface roughness parameter for spaceborne GNSS-R data. Nonetheless, the analysis of different GNSS constellations obtained consistent results. These findings will pave the way for subsequent collaborative use of multi-GNSS constellation reflection measurements for multiparameter retrieval and fusion of reflection measurements from different spaceborne GNSS-R satellites.

References

[1] C. D. Hall and R. A. Cordey, "Multistatic scatterometry," in *Proc. Int. Geosci. Remote Sens. Symp., Moving Toward 21st Century*, 1988, vol. 1, pp. 561–562, doi: 10.1109/IGARSS.1988.570200.

[2] J. C. Auber, A. Bibaut, and J. M. Rigal, "Characterization of multipath on land and sea at GPS frequencies," in *Proc. 7th Int. Tech. Meeting Satell. Division Inst. Navig.*, 1994, pp. 1155–1171. [Online]. Available: https://www.ion.org/publications/abstract.cfm?articleID=4024

[3] M. Martín-Neira, "A passive reflectometry and interferometry system (PARIS): Application to ocean altimetry," *ESA J.*, vol. 17, no. 4, pp. 331–355, 1993.

[4] S. J. Katzberg and J. L. Garrison, "Utilizing GPS to determine ionospheric delay over the ocean," NASA Tech. Memorandum, 4750, Dec. 1996. [Online]. Available: https://ntrs.nasa.gov/citations/19970005019

[5] J. L. Garrison and S. J. Katzberg, "Detection of ocean reflected GPS signals: Theory and experiment," in *Proc. IEEE Southeastcon Conf.*, Blacksburg, VA, USA, 1997, pp. 290–294, doi: 10.1109/SECON.1997.598694.

[6] S. T. Lowe, J. L. LaBrecque, C. Zuffada, L. J. Romans, L. E. Young, and G. A. Hajj, "First spaceborne observation of an Earth-reflected GPS signal," *Radio Sci.*, vol. 37, no. 1, pp. 7–1–7–28, 2002, doi: 10.1029/2000RS002539.

[7] S. Gleason et al., "Detection and processing of bistatically reflected GPS signals from low Earth orbit for the purpose of ocean remote sensing," *IEEE Trans. Geosci. Remote Sens.*, vol. 43, no. 6, pp. 1229–1241, Jun. 2005, doi: 10.1109/TGRS.2005.845643.

[8] M. Unwin, P. Jales, J. Tye, C. Gommenginger, G. Foti, and J. Rosello, "Spaceborne GNSS-reflectometry on TechDemoSat-1: Early mission operations and exploitation," *IEEE J. Sel. Topics Appl. Earth Observ. Remote Sens.*, vol. 9, no. 10, pp. 4525–4539, Oct. 2016, doi: 10.1109/JSTARS.2016.2603846.

[9] M. Clarizia, C. Gommenginger, S. Gleason, C. Galdi, and M. Unwin, "Global navigation satellite system-reflectometry (GNSS-R) from the U.K.-DMC satellite for remote sensing of the ocean surface," in *Proc. IGARSS IEEE Int. Geosci. Remote Sens. Symp.*, 2008, pp. I–276–I–279, doi: 10.1109/IGARSS.2008.4778847.

[10] A. Camps et al., "Sensitivity of GNSS-R spaceborne observations to soil moisture and vegetation," *IEEE J. Sel. Topics Appl. Earth Observ. Remote Sens.*, vol. 9, no. 10, pp. 4730–4742, Oct. 2016, doi: 10.1109/JSTARS.2016.2588467.

[11] A. Alonso-Arroyo, V. U. Zavorotny, and A. Camps, "Sea ice detection using U.K. TDS-1 GNSS-R data," *IEEE Trans. Geosci. Remote Sens.*, vol. 55, no. 9, pp. 4989–5001, Sep. 2017, doi: 10.1109/TGRS.2017.2699122.

[12] C. Ruf et al., "New ocean winds satellite mission to probe hurricanes and tropical convection," *Bull. Amer. Meteorol. Soc.*, vol. 97, pp. 385–395, 2016, doi: 10.1175/BAMS-D-14-00218.1.

[13] H. Carreno-Luengo et al., "3Cat-2—An experimental nanosatellite for GNSS-R Earth observation: Mission concept and analysis," *IEEE J. Sel. Topics Appl. Earth Observ. Remote Sens.*, vol. 9, no. 10, pp. 4540–4551, Oct. 2016, doi: 10.1109/JSTARS.2016.2574717.

[14] A. Camps et al., "FSSCat: The federated satellite systems 3Cat mission: Demonstrating the capabilities of CubeSats to monitor essential climate variables of the water cycle [Instruments and missions]," *IEEE Geosci. Remote Sens. Mag.*, vol. 10, no. 4, pp. 260–269, Dec. 2022, doi: 10.1109/MGRS.2022.3219778.

[15] C. Jing, X. Niu, C. Duan, F. Lu, G. Di, and X. Yang, "Sea surface wind speed retrieval from the first Chinese GNSS-R mission: Technique and preliminary results," *Remote Sens.*, vol. 11, no. 24, Dec. 2019, Art. no. 3013, doi: 10.3390/rs11243013.

[16] C. Ruf and R. Balasubramaniam, "Development of the CYGNSS geophysical model function for wind speed," *IEEE J. Sel. Topics Appl. Earth Observ. Remote Sens.*, vol. 12, no. 1, pp. 66–77, Jan. 2019, doi: 10.1109/JSTARS.2018.2833075.

[17] W. Li, E. Cardellach, F. Fabra, S. Ribo, and A. Rius, "Assessment of spaceborne GNSS-R ocean altimetry performance using CYGNSS mission raw data," *IEEE Trans. Geosci. Remote Sens.*, vol. 58, no. 1, pp. 238–250, Jan. 2020, doi: 10.1109/TGRS.2019.2936108.

[18] C. C. Chew and E. E. Small, "Soil moisture sensing using spaceborne GNSS reflections: Comparison of CYGNSS reflectivity to SMAP soil moisture," *Geophys. Res. Lett.*, vol. 45, no. 9, pp. 4049–4057, May 2018, doi: https://doi.org/10.1029/2018GL077905.

[19] H. Kim and V. Lakshmi, "Use of cyclone global navigation satellite system (CyGNSS) observations for estimation of soil moisture," *Geophys. Res. Lett.*, vol. 45, no. 16, pp. 8272–8282, Aug. 2018, doi: 10.1029/2018GL078923.

[20] M. P. Clarizia, N. Pierdicca, F. Costantini, and N. Floury, "Analysis of CYGNSS data for soil moisture retrieval," *IEEE J. Sel. Topics Appl. Earth Observ. Remote Sens.*, vol. 12, no. 7, pp. 2227–2235, Jul. 2019, doi: 10.1109/JSTARS.2019.2895510.

[21] Q. Yan, W. Huang, S. Jin, and Y. Jia, "Pan-tropical soil moisture mapping based on a three-layer model from CYGNSS GNSS-R data," *Remote Sens. Environ.*, vol. 247, Sep. 2020, Art. no. 111944, doi: 10.1016/j.rse.2020.111944.

[22] H. Carreno-Luengo, G. Luzi, and M. Crosetto, "Above-ground biomass retrieval over tropical forests: A novel GNSS-R approach with CyGNSS," *Remote Sens.*, vol. 12, no. 9, Apr. 2020, Art. no. 1368, doi: 10.3390/rs12091368.

[23] E. Santi et al., "Remote sensing of forest biomass using GNSS reflectometry," *IEEE J. Sel. Topics Appl. Earth Observ. Remote Sens.*, vol. 13, pp. 2351–2368, May 2020, doi: 10.1109/JSTARS.2020.2982993.

[24] M. Morris, C. Chew, J. T. Reager, R. Shah, and C. Zuffada, "A novel approach to monitoring wetland dynamics using CYGNSS: Everglades case study," *Remote Sens. Environ.*, vol. 233, Nov. 2019, Art. no. 111417, doi: 10.1016/j.rse.2019.111417.

[25] C. Chew, E. Small, and H. Huelsing, "Flooding and inundation maps using interpolated CYGNSS reflectivity observations," *Remote Sens. Environ.*, vol. 293, Aug. 2023, Art. no. 113598, doi: 10.1016/j.rse.2023.113598.

[26] J. Zhang and Y. J. Morton, "Inland water body surface height retrievals using CYGNSS delay Doppler maps," *IEEE Trans. Geosci. Remote Sens.*, vol. 61, Nov. 2023, Art. no. 4209316, doi: 10.1109/TGRS.2023.3330410.

[27] C. Chew, J. T. Reager, and E. Small, "CYGNSS data map flood inundation during the 2017 Atlantic hurricane season," *Sci. Rep.*, vol. 8, no. 1, Jun. 2018, Art. no. 9336, doi: 10.1038/s41598-018-27673-x.

[28] W. Wan et al., "Using CYGNSS data to monitor China's flood inundation during typhoon and extreme precipitation events in 2017," *Remote Sens.*, vol. 11, no. 7, Apr. 2019, Art. no. 854, doi: 10.3390/rs11070854.

[29] Z. Ma et al., "Using CYGNSS and L-band radiometer observations to retrieve surface water fraction: A case study of the catastrophic flood of 2022 in Pakistan," *IEEE Trans. Geosci. Remote Sens.*, vol. 62, Feb. 2024, Art. no. 4203117, doi: 10.1109/TGRS.2024.3367491.

[30] X. Wu, "First measurement of soil freeze/thaw cycles in the Tibetan Plateau using CYGNSS GNSS-R data," *Remote Sens.*, vol. 12, no. 5, 2020, Art. no. 2361, doi: 10.3390/rs12152361.

[31] H. Carreno-Luengo and C. S. Ruf, "Retrieving freeze/thaw surface state from CYGNSS measurements," *IEEE Trans. Geosci. Remote Sens.*, vol. 60, Oct. 2022, Art. no. 4302313, doi: 10.1109/TGRS.2021.3120932.

[32] D. Comite, L. Cenci, A. Colliander, and N. Pierdicca, "Monitoring freeze-thaw state by means of GNSS reflectometry: An analysis of TechDemoSat-1 data," *IEEE J. Sel. Topics Appl. Earth Observ. Remote Sens.*, vol. 13, pp. 2996–3005, May 2020, doi: 10.1109/JSTARS.2020.2986859.

[33] W. Li, E. Cardellach, S. Ribó, S. Oliveras, and A. Rius, "Exploration of multi-mission spaceborne GNSS-R raw IF data sets: Processing data products and potential applications," *Remote Sens.*, vol. 14, no. 6, Mar. 2022, Art. no. 1344, doi: 10.3390/rs14061344.

[34] Q. Liu et al., "Analysis of signal-to-noise ratio retrieved from multi-GNSS satellite data of land surface reflections," *GPS Solutions*, vol. 27, Jun. 2023, Art. no. 151, doi: 10.1007/s10291-023-01502-9.

[35] Y. Sun et al., "GNOS-II on Fengyun-3 satellite series: Exploration of multi-GNSS reflection signals for operational applications," *Remote Sens.*, vol. 15, no. 24, Dec. 2023, Art. no. 5756, doi: 10.3390/rs15245756.

[36] G. Yang et al., "FY3E GNOS II GNSS reflectometry: Mission review and first results," *Remote Sens.*, vol. 14, no. 4, Feb. 2022, Art. no. 988, doi: 10.3390/rs14040988.

[37] FY-3E GNOS-II L1 Data (GNSS-R) Version 0, Nat. Satell. Meteorol. Center, Beijing, China, 2024. [Online]. Available: https://satellite.nsmc.org.cn/PortalSite/Data/Satellite.aspx?currentculture=en-US

[38] C. Yin et al., "Soil moisture retrieval from multi-GNSS reflectometry on FY-3E GNOS-II by land cover classification," *Remote Sens.*, vol. 15, no. 4, Feb. 2023, Art. no. 1097, doi: 10.3390/rs15041097.

[39] N. N. Das et al., "The SMAP and Copernicus Sentinel 1A/B microwave active-passive high resolution surface soil moisture product," *Remote Sens. Environ.*, vol. 233, 2019, Art. no. 111380, doi: 10.1016/j.rse.2019.111380.

[40] SMAP Enhanced L3 Radiometer Global and Polar Grid Daily 9 Km EASE-Grid Soil Moisture Version 5, NASA Nat. Snow Ice Data Center Distrib. Active Arch. Center, Boulder, CO, USA, 2024. [Online]. Available: https://doi.org/10.5067/4DQ54OUIJ9DL

[41] Soil Moisture Active Passive (SMAP) L1-L3 Ancillary Static Data V001. Version 1, Nat. Aeronaut. Space Admin., U.S. Government, NASA Nat. Snow Ice Data Center Distrib. Active Arch. Center, n.d. [Online]. Available: https://doi.org/10.5067/HB8BPJ13TDQJ

[42] J. Chaubell et al., "Analysis of the SMAP roughness parameter and the SMAP vegetation optical depth," in *Proc. IEEE Int. Geosci. Remote Sens. Symp.*, Kuala Lumpur, Malaysia, 2022, pp. 4232–4235, doi: 10.1109/IGARSS46834.2022.9883263.

[43] B. Hornbuckle, V. Walker, B. Eichinger, V. Wallace, and E. Yildirim, "Soil surface roughness observed during SMAPVEX16-IA and its potential consequences for SMOS and SMAP," in *Proc. IEEE Int. Geosci. Remote Sens. Symp.*, 2017, pp. 2027–2030, doi: 10.1109/IGARSS.2017.8127379.

[44] S. H. Yueh, R. Shah, M. J. Chaubell, A. Hayashi, X. Xu, and A. Colliander, "A semiempirical modeling of soil moisture, vegetation, and surface roughness impact on CYGNSS reflectometry data," *IEEE Trans. Geosci. Remote Sens.*, vol. 60, Nov. 2020, Art. no. 5800117, doi: 10.1109/TGRS.2020.3035989.

[45] V. Walker, B. Hornbuckle, M. Cosh, and J. Prueger, "Seasonal evaluation of SMAP soil moisture in the US corn belt," *Remote Sens.*, vol. 11, 2019, Art. no. 2488, doi: 10.3390/rs11212488.

[46] M. Parrens et al., "Global-scale surface roughness effects at L-band as estimated from SMOS observations," *Remote Sens. Environ.*, vol. 181, pp. 122–136, 2016, doi: 10.1016/j.rse.2016.04.006.

[47] A. Camps, H. Park, J. Castellví, J. Corbera, and E. Ascaso, "Single-pass soil moisture retrievals using GNSS-R: Lessons learned," *Remote Sens.*, vol. 12, no. 12, Jun. 2020, Art. no. 2064, doi: 10.3390/rs12122064.

[48] J.-P. Wigneron et al., "SMOS-IC data record of soil moisture and L-VOD: Historical development applications and perspectives," *Remote Sens. Environ.*, vol. 254, 2021, Art. no. 112238, doi: 10.1016/j.rse.2020.112238.

[49] X. Li et al., "The first global soil moisture and vegetation optical depth product retrieved from fused SMOS and SMAP L-band observations," *Remote Sens. Environ.*, vol. 282, 2022, Art. no. 113272, doi: 10.1016/j.rse.2022.113272.

[50] X. Li et al., "Global-scale assessment and inter-comparison of recently developed/reprocessed microwave satellite vegetation optical depth products," *Remote Sens. Environ.*, vol. 253, 2021, Art. no. 112208, doi: 10.1016/j.rse.2020.112208.

[51] J.-P. Wigneron et al., "Global carbon balance of the forest: Satellite-based L-VOD results over the last decade," *Front. Remote Sens.*, vol. 5, 2024, Art. no. 1338618, doi: 10.3389/frsen.2024.1338618.

[52] SMOS IC L-VOD Version 2.0 INRAE, UMR1391 ISPA, Université de Bordeaux, Villenave d'Ornon, France, n.d. [Online]. Available: https://ib.remote-sensing.inrae.fr/

[53] M. Al-Khaldi et al., "Inland water body mapping using CYGNSS coherence detection," *IEEE Trans. Geosci. Remote Sens.*, vol. 59, no. 9, pp. 7385–7394, Sep. 2021, doi: 10.1109/TGRS.2020.3047075.

[54] H. Carreno-Luengo et al., "Detection of inland water bodies under dense biomass by CYGNSS," *Remote Sens. Environ.*, vol. 301, Feb. 2024, Art. no. 113896, doi: 10.1016/j.rse.2023.113896.

[55] M. M. Al-Khaldi, R. Shah, C. C. Chew, J. T. Johnson, and S. Gleason, "Mapping the dynamics of the South Asian monsoon using CYGNSS's level-1 signal coherency," *IEEE J. Sel. Topics Appl. Earth Observ. Remote Sens.*, vol. 14, pp. 1111–1119, Dec. 2020, doi: 10.1109/JSTARS.2020.3042170.

[56] N. Pierdicca, L. Guerriero, M. Brogioni, and A. Egido, "On the coherent and non-coherent components of bare and vegetated terrain bistatic scattering: Modelling the GNSS-R signal over land," in *Proc. IEEE Int. Geosci. Remote Sens. Symp.*, Munich, Germany, 2012, pp. 3407–3410, doi: 10.1109/IGARSS.2012.6350689.

[57] R. D. De Roo and F. T. Ulaby, "Bistatic specular scattering from rough dielectric surfaces," *IEEE Trans. Antennas Propag.*, vol. 42, no. 2, pp. 220–231, Feb. 1994, doi: 10.1109/8.277216.

[58] G. Yang et al., "An illustration of FY-3E GNOS-R for global soil moisture monitoring," *Sensors*, vol. 23, no. 13, Jun. 2023, Art. no. 5825, doi: 10.3390/s23135825.

[59] Y. H. Kerr et al., "The SMOS soil moisture retrieval algorithm," *IEEE Trans. Geosci. Remote Sens.*, vol. 50, no. 5, pp. 1384–1403, May 2012, doi: 10.1109/TGRS.2012.2184548.

[60] H. Park, A. Camps, J. Castellvi, and J. Muro, "Generic performance simulator of spaceborne GNSS-reflectometer for land applications," *IEEE J. Sel. Topics Appl. Earth Observ. Remote Sens.*, vol. 13, pp. 3179–3191, Jun. 2020, doi: 10.1109/JSTARS.2020.3000391.

[61] C. Chew and E. Small, "Estimating inundation extent using CYGNSS data: A conceptual modeling study," *Remote Sens. Environ.*, vol. 246, Sep. 2020, Art. no. 111869, doi: 10.1016/j.rse.2020.111869.

[62] J. F. Munoz-Martin et al., "Single-pass soil moisture retrieval using GNSS-R at L1 and L5 bands: Results from airborne experiment," *Remote Sens.*, vol. 13, no. 4, 2021, Art. no. 797, doi: 10.3390/rs13040797.

[63] N. Pierdicca et al., "Potential of spaceborne GNSS reflectometry for soil moisture biomass and freeze-thaw monitoring: Summary of an ESA-funded study," *IEEE Geosci. Remote Sens. Mag.*, vol. 10, no. 2, pp. 8–38, Jun. 2022, doi: 10.1109/MGRS.2021.3115448.

[64] J. F. Munoz-Martin, N. Rodriguez-Alvarez, X. Bosch-Lluis, and K. Oudrhiri, "Analysis of polarimetric GNSS-R stokes parameters of the Earth's land surface," *Remote Sens. Environ.*, vol. 287, Mar. 2023, Art. no. 113491, doi: 10.1016/j.rse.2023.113491.

[65] J. F. Munoz-Martin, N. Rodriguez-Alvarez, X. Bosch-Lluis, and K. Oudrhiri, "Effective surface roughness impact in polarimetric GNSS-R soil moisture retrievals," *Remote Sens.*, vol. 15, no. 8, Apr. 2023, Art. no. 2013, doi: 10.3390/rs15082013.

[66] H. Carreno-Luengo, G. Luzi, and M. Crosetto, "Impact of the elevation angle on CYGNSS GNSS-R bistatic reflectivity as a function of effective surface roughness over land surfaces," *Remote Sens.*, vol. 10, no. 11, Nov. 2018, Art. no. 1749, doi: 10.3390/rs10111749.

[67] John William Strutt Baron Rayleigh, *The Theory of Sound*, vol. 2. New York, NY, USA: Macmillan, 1896.

[68] S. Rahman et al., "Agriculture flood mapping with soil moisture active passive (SMAP) data: A case of 2016 Louisiana flood," in *Proc. 6th Int. Conf. Agro-Geoinform.*, 2017, pp. 1–6, doi: 10.1109/Agro-Geoinformatics.2017.8047062.

Zhongmin Ma (Student Member, IEEE) received the B.S. degree in surveying and mapping engineering from Chang'an University, Xi'an, China, in 2019 where he is currently working toward the Ph.D. degree in surveying and mapping with the College of Geological Engineering and Geomatics. He is also currently working toward the joint Ph.D. degree in surveying and mapping with CommSensLab, Universitat Politècnica de Catalunya, Barcelona, Spain, as a China Scholarship Council.

His research focuses on global navigation satellite system remote sensing and its applications to floods and land surface water.

Adriano Camps (Fellow, IEEE) received the degree in telecommunications engineering from the School of Telecommunications Engineering, Universitat Politecnica de Catalunya, Barcelona, Spain, in 1992, and the Ph.D. degree in telecommunications engineering from the Universitat Politecnica de Catalunya, in 1996.

He joined the CommSensLab-Universitat Politècnica de Catalunya (UPC) Group, Department of Signal Theory and Communications, UPC, Barcelona, Spain, as an Assistant Professor in 1993, an Associate Professor in 1997, and has been a Full Professor since 2007. In 1999, he was on sabbatical leave with Microwave Remote Sensing Laboratory, University of Massachusetts at Amherst, Amherst, MA, USA. He has authored or coauthored more than 285 articles published in peer-reviewed journals, 9 book chapters, the book with "Emery Introduction to Satellite Remote Sensing: Atmosphere, Ocean, Land and Cryosphere Applications" (Elsevier, 2017), and more than 559 conference presentations. His h-index is 64/51, and his publications have received more than 16.905/11.531 citations, and has advised 33 Ph.D. thesis students (more than ten ongoing) and more than 160 final projects and M.Eng. theses.

Dr. Camps was the recipient of several awards, including the European Young Investigator Award in 2004 (ERC precursor), the Catalan Institution for Research and Advanced Studies Academia Research Award in 2009 and 2015, the Duran Farell Award for Technology Transfer in 2000, 2010, and 2022, and the 2021 IEEE GRSS Education Award.

Hyuk Park (Senior Member, IEEE) was born in South Korea. He received the B.S. degree in mechanical engineering from the Korea Advanced Institute of Science and Technology, Daejeon, South Korea, in 2001, and the M.S. and Ph.D. degrees in information and mechatronics from the Gwangju Institute of Science and Technology, Gwangju, South Korea, in 2003 and 2009, respectively.

In 2009, he joined Remote Sensing Group with the Polytechnic University of Catalonia (UPC), Barcelona, Spain, as a Postdoctoral Researcher. Since 2012, he has been a Researcher with Juan de la Cierva grant and, since 2018, as a Ramon y Cajal Fellow funded by the Spanish Ministry of Economy and Competitiveness. He is currently an Associate Professor with the School of Telecommunications and Aerospace Engineering, Castelldefels (EETAC-UPC), Barcelona, Spain. He is also a part of Passive Remote Sensing Group with UPC, specializing in satellite remote sensing for microwave radiometry and global navigation satellite systems reflectometry. His main research interests include remote sensing, particularly passive microwave remote sensing, covering system design, modeling and simulation, image/data processing, and small satellite applications in positioning, navigation, and timing and communications.

Shuangcheng Zhang received the Ph.D. degree in geodesy from Wuhan University, Wuhan, China, in 2009.

He is currently a Professor with Chang'an University, Xi'an, China. His research focuses on the study of geodynamics and global navigation satellite system remote sensing.

Xiaojun Li received the Ph.D. degree in environmental physics from the University of Bordeaux, Bordeaux, France, in 2022.

He is currently a Postdoctoral Researcher with INRAE Bordeaux (2022–present), working under the supervision of Jean-Pierre Wigneron on analyzing global carbon stock changes from disturbance using IB L-VOD. During his Ph.D., he developed the SMOS-IC version 2/SMAP-IB retrieval product and is currently responsible for evaluating and releasing the IB *L*-band SM and VOD products. His research interests include microwave soil moisture retrieval models, validation, and carbon cycle estimation. He has authored or coauthored >60 papers in top-tier journals, such as NCC, RSE, and JOH. His current work is funded by RECCAP2 Project, which is a part of ESA Climate Change Initiative (Contract no. 4000123002/18/I-NB).

Jean-Pierre Wigneron (Fellow, IEEE) received the M.Sc. degree in engineering from the Ecole Nationale Supérieure de l'Aéronautique et de l'Espace, Toulouse, France, in 1987, and the Ph.D. degree in remote sensing from the University of Toulouse, Toulouse, France, in 1993.

He is currently a Senior Research Scientist with ISPA, INRAE, Bordeaux, France, where he is the Head of INRAE Bordeaux IB Remote Sensing Lab. He has authored or coauthored more than 300 papers in international peer-reviewed journals, >20 in Nature and Science Journals, and >50 in Remote Sensing of Environment. He has developed pioneer work in the simultaneous retrievals of soil moisture and vegetation biomass from passive microwave remote sensing observations and developed the L-MEB model, the forward model of operational algorithms of the European Space Agency SMOS satellite mission. His research interests include the use of passive and active microwave remote sensing to monitor the carbon and water cycles of forest areas at national/continental scales. He is a Highly Cited Researcher 2021 (Clarivate Analytics), a member of the Scientific Committee of the French Remote Sensing Data Center (Theia), has been an Associate Editor for the *Remote Sensing of Environment* from 2014 to 2022, and is the Field Chief Editor for *Frontiers in Remote Sensing*.